ELSEVIER

Chemical Engineering Journal 140 (2008) 332–340

Chemical Engineering Journal

www.elsevier.com/locate/cej

Liquid flow texture analysis in trickle bed reactors using high-resolution gamma ray tomography

Markus Schubert [a,*], Günther Hessel [a], Cornelius Zippe [a], Rüdiger Lange [b], Uwe Hampel [a]

[a] *Institute of Safety Research, Research Center Forschungszentrum Dresden-Rossendorf e.V., POB 51 01 19, 01314 Dresden, Germany*
[b] *Department of Chemical Engineering, Dresden University of Technology, 01062 Dresden, Germany*

Received 8 August 2007; received in revised form 4 October 2007; accepted 5 October 2007

Abstract

Trickle bed reactor performance and safety may suffer from radial and axial liquid maldistribution and thus from non-uniform utilization of the catalyst packing. Therefore, experimental analysis and fluid dynamic simulation of liquid–gas flow in trickle bed reactors is an important topic in chemical engineering. In the present study for the first time a truly high-resolution gamma ray tomography technique was applied to the quantitative analysis of the liquid flow texture in a laboratory cold flow trickle bed reactor of 90 mm diameter. The objective of this study was to present the comparative analysis of the liquid flow dynamics for two different initial liquid distributions and two different types of reactor configurations. Thus, the hydrodynamic behavior of a glass bead packing was compared to a porous Al_2O_3 catalyst particle packing using inlet flow from a commercial spray nozzle (uniform initial liquid distribution) and inlet flow from a central point source (strongly non-uniform initial liquid distribution), respectively. The column was operated in downflow mode at a gas flow rate of 180 L h^{-1} and at liquid flow rates of 15 and 25 L h^{-1}.

Keywords: Gamma ray tomography; Multiphase flow; Trickle bed; Liquid saturation; Liquid distribution; Liquid spreading

1. Introduction

Multiphase flows exist in many areas of commerce such as the manufacture of petroleum-based products and fuels, the production of commodity and specialty chemicals, pharmaceuticals, production of polymers and pollution abatement, as well as for distillation and absorption in separation applications. Randomly packed beds operated in gas–liquid concurrent downflow mode in the trickling regime form an essential part of multiphase reactors and are widely used for hydrotreating, hydrocracking, hydrodesulphurization, and oxidation reactions in the chemical, biochemical and waste treatment industry [1,2]. There are several advantages to the downflow mode, including a wide operating window for gas/liquid flow rates, high gas/liquid interaction, as well as low pressure drops, high capacities and high efficiencies. However, non-uniform liquid distribution due to improper initial gas/liquid distributors, external bed porosity variations, wall effects, partial catalyst wetting and surface tension related effects has a detrimental influence on reactor performance. In particular, non-uniform liquid distribution leads to a decrease in catalyst utilization, development of radial and axial temperature profiles and hazardous hot-spots, catalyst deactivation and a decrease in conversion, selectivity and production rates. For instance, bypassing or strongly channeling liquids in deep hydrodesulphurization can lead to a sulfur content which exceeds legal standards [3].

Hence, it can be concluded that hydrodynamics such as saturation, pressure drop, and liquid distribution are fundamental criteria for the selection and productivity of multiphase reactors [4]. One of the most important hydrodynamic quantities for the design, scale-up, and modeling of trickle bed reactors is the liquid saturation, which, in simplified form, is the ratio of the liquid volume to the bed voidage. The liquid saturation permits the prediction of the pressure drop as well as the calculation of the effective liquid velocity within the packing, which is in turn related to heat and mass transfer parameters and other hydrodynamic quantities such as wetting efficiency and residence time distribution. In the end, it is essential to determine phase holdup profiles, external bed porosity distribution and spatial flow patterns and their deviation from ideal plug flow in order to develop

* Corresponding author. Tel.: +49 351 260 2627; fax: +49 351 260 2383.
E-mail address: m.schubert@fzd.de (M. Schubert).

1385-8947/$ – see front matter © 2007 Elsevier B.V. All rights reserved.
doi:10.1016/j.cej.2007.10.006

Nomenclature

a	geometric contribution
cps	counts per second
d	diameter (m)
E	linear extinction
h	slice height index
l	length of resolution element (m)
n_D	number of detector
n_P	number of projections
N	number of photoabsorbed gamma photons
n_x	number of pixels in x direction
n_y	number of pixels in y direction
r	radius (m)
th	threshold

Greek letters

β	liquid saturation
φ	projection angle
λ	relaxation factor
μ	attenuation coefficient
ν	valitity mask values
τ	iteration number
θ	angle coordinate

Subscripts

i	pixel index
int	integral
j	pixel index
k	detector number
l	index of the projection
m	protection number
R	reactor

Superscripts

d	dark
dyn	dynamic
stat	static
tot	total

and to validate mathematical models concerning heterogeneous flow texture [5].

Multiphase flows, especially in randomly packed beds of porous media, are difficult to visualize and characterize due to the opaque nature of the systems. Conventional measurement methods which are widely available today include differential pressure measurement at inlet and outlet [6], tracer transport measurement [7] and local sensors, such as temperature and pressure transducers as well as phase indicator sensors [8,9], inserted at selected locations in the bed. Such measurement techniques mainly give a global view on the reactor performance; however, many small-scale details which actually dominate system outcomes as well as reactor safety and which need to be understood for proper system characterization cannot be assessed.

Attempts have been made in the past to introduce tomographic imaging techniques to the study of trickle bed reactor hydrodynamics. One choice is nuclear magnetic resonance imaging (MRI), which has been successfully introduced by Gladden et al. [10] and Koptyug et al. [11]. MRI is able to provide information on phase fraction distribution and even chemical information at high spatial and temporal resolution. Its major problem lies in its non-applicability to reactors with steel walls which are commonly used in pressurized catalytic multiphase systems. Another potential tomographic imaging modality is electrical impedance tomography [12]. Here, electrical conductivity, respectively, permittivity patterns inside the reactor bed are measured with a multi-electrode probing-sensing scheme. Though simple in concept and conceptually fast this technique provides only limited spatial resolution which even decreases towards the center of the bed. Thus, only little flow texture detail can be revealed. Radiation attenuation measurement techniques, as applied in this study, have the capability to overcome the limits of the above mentioned techniques [13]. Candidates for such a technique are X-ray tomography and gamma ray tomography. Gamma ray computed tomography (CT) is better suited when high radiation energy is needed, e.g. in the case of large reactor diameters, dense packing and in the case of steel walls and steel facilities for pressurized operation. In this case, Cs-137 sources with 662 keV photon energy or Co-60 sources with 1117 and 1333 keV photon energy are applicable. Achieving a comparable energy with X-ray sources requires the application of accelerator based systems which are bulky and expensive and cannot be applied outside specially equipped laboratories. A particular problem of gamma ray tomography systems is the achievement of high spatial resolution. Since the photon flux of isotopic sources is limited, typically to a few hundred photons/(mm^2 s) at 1 m distance, an efficient detector design is required. In most gamma ray CT devices this has been achieved by using large Bismuth Germanate (BGO) or CsI(Tl) crystals coupled to photomultiplier tubes [14–19]. Such arrangements, however, have clear limits regarding spatial resolution. Recently, our group has developed a high-resolution gamma ray CT system based on a novel detector technology using Lutetium Yttrium Orthosilicate (LYSO) crystals and large area avalanche photodiodes. The system will be described in more detail in the next section. In the following section the paper continues with a brief discussion of the few gamma ray tomography studies employed in trickle flows which have been published.

Harter et al. [3] measured qualitatively the external bed porosity of a granular medium and the liquid distribution 4.7 m downstream from the distributor in a 5 m height mock-up unit of 60 cm diameter with a gamma ray scanner. Increasing homogeneity of the radial liquid distribution from a central inlet stream (50 mm inlet tube) to an optimized distributor was demonstrated. Results from the central inlet stream showed that poor initial liquid dispersion cannot be subsequently recovered by reactor length. Boyer and Fanget [20] measured the external bed porosity to slightly higher values in the wall zone due to the nature of their loading procedure. Sensitivity of the equipment to non-uniform initial liquid distribution was checked with a liquid distributor of four concentric zones which can be activated

separately. Measurements of the liquid distribution performed 1 m downstream from the distributor display non-annulus variations in the liquid distribution which were attributed to the catalyst bed structure, which would be impossible to deduce from the given external bed porosity image. Boyer et al. [21] focused on liquid spreading from a point source in a trickle bed reactor with a length of 1.80 m and a diameter of 0.4 m. They studied the effect of gas flow rate and pre-wetting conditions on spreading angle and spreading length in a packing of spherical glass beads, but the effect of liquid flow rate and different packing characteristics (e.g. particle diameter as mentioned in the introduction) failed to appear. Liquid spreading study indicated nearly radial-symmetric behavior. Tomographic measurements of the cross-sectional liquid distribution are limited to three heights and thus the axial jet contour database for validation of Computational Fluid Dynamics (CFD) models as proposed by Boyer et al. [21] is low.

Gamma ray tomography was also used by Wang et al. [22] to measure the external bed porosity of a high efficiency stainless steel pall ring packing in a reactor of 6 m length and 0.6 m diameter. Radial external bed porosity profiles of the dense packing did not show any oscillatory patterns such as those found for spherical particles. Higher porosity values in the wall region agree with results of Boyer and Fanget [20]. Yin et al. [23] continued the porosity study of Wang et al. [22] with liquid holdup measurements for different distributors at two different heights. If central introduction of the liquid is carried out as an extreme case then, due to low spreading angle the liquid does not reach the reactor wall within a length of reactor diameter. Despite the application of a uniform distributor at the top of the reactor, spatial variations in the liquid holdup values were observed. In general, lower holdup values at the wall are in agreement with higher external bed porosity in this region and identify liquid holdup distribution as a function of the external bed porosity.

In the present work, liquid saturation distribution has been investigated for a uniform initial liquid distribution realized by a spray nozzle. Liquid saturation results are differentiated into the corresponding dynamic and static fractions. As variation of liquid saturation is attributed to the void fraction between the particles, external bed porosity was considered, too. Additional liquid spreading from a point source has been measured. Tomographic images were recorded at six different heights downstream from the top of the packing to analyze axial variations. In all cases, two different liquid flow rates were adjusted. As previous liquid spreading results show a lack of data obtained for porous packing material, the effect of packing material was investigated using non-porous glass beads and a real catalyst packing of porous spherical particles of similar size.

The data presented can be used to validate and improve liquid distribution and liquid spreading models, e.g. the cellular automated model recently published by Alopaeus et al. [24] or the conceptual pore level model [25].

2. Experimental setup and processing

2.1. Trickle bed reactor setup

The experimental setup employed in the experiments is outlined in Fig. 1. An acrylic trickle bed reactor with a diameter of 0.09 m and a height of 0.60 m was randomly packed with commercial porous γ-Al_2O_3 catalyst spheres for selective hydrogenation of acetylenic bonds and diolefins and glass beads, respectively, each of 4.0 mm diameter which gives a ratio of reactor over particle diameter greater than 20. The specification of the catalyst is summarized in Table 1.

Volumetric flow rates of the liquid phase (water) were adjusted to 15 and 25 L h^{-1} corresponding to the trickle flow regime. Due to the necessary acquisition time tomographic

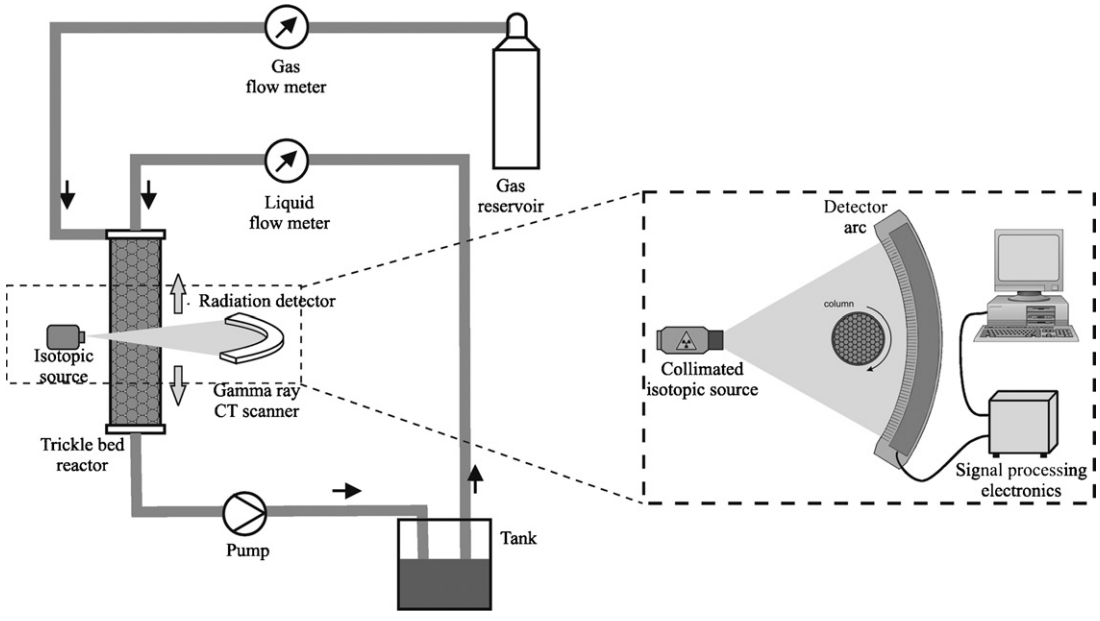

Fig. 1. Experimental setup including trickle bed reactor and gamma ray tomograph.

Table 1
Specification of the catalyst

Properties	Unit	Value
Active metal	–	Palladium
Active metal content	wt.%	0.3
Catalyst support	–	Al_2O_3
Packing shape	–	Spherical pellets
Average diameter	mm	4.0 mm
Total surface area (BET)	$m^2\,g^{-1}$	90
Specific pore volume	$mL\,g^{-1}$	0.65
Bulk density	$kg\,m^{-3}$	750

imaging of liquid flow requires steady state flow without variations of phase fractions and their locations during measurement time. For that reason, a proper pre-wetting procedure was realized in order to guarantee stable flow patterns for a longer period of time. It was shown by van der Merwe et al. [26] that trickle flow is stable in all but the Levec pre-wetting mode for porous alumina catalyst particles. Additionally, their radiographic images indicated that the liquid saturation stabilizes shortly after the end of the start-up procedure for all pre-wetted beds. No local saturation changes had been identified. As a pre-wetting mode, super pre-wetting (liquid introduction initiated simultaneously with draining after last flooding with an ascending flow) was used. Pressurized air provided by the house installation was used as the gas phase at a nominal volumetric flow rate of $180\,L\,h^{-1}$. Flow rates corresponded to the trickle flow regime. The gas and liquid were supplied concurrently at the top of the reactor and adjusted by a mass flow controller (Bronkhorst, F-201C-FB-33-V) and a rotameter (Prüfgerätewerk Medingen, $2–25\,L\,h^{-1}$, H_2O), respectively. The gas phase was delivered via a non-central hole in the top flange of the reactor. The liquid phase was delivered via a single central point source in the top flange to study liquid spreading, and via a commercial spray nozzle (VKL-0.6-90-G1/8-MS, Spraying System), designed for the flow rate range investigated, to study the hydrodynamics at uniform initial distribution conditions, respectively.

The brass spray nozzle is mainly used for washing and rinsing applications as well as for irrigation of packings. Manufacturers' instructions predict a full cone spray angle of 90° at a maximal free passage of 0.45 mm. The pressure drop is approximately 0.75 bar at a capacity of $15\,L\,h^{-1}$ and 2.0 bar at $25\,L\,h^{-1}$. From optical examination of the liquid spraying process a spraying angle of 82° was determined from which a clear distance of 50 mm between packing and the spray nozzle was inferred to ensure a uniform initial distribution.

2.2. Gamma ray tomography setup

The gamma ray tomography setup employed in the experiments is schematically illustrated in Fig. 1. The isotopic source is a Cs-137 radiator with 662 keV photon energy and approximately 160 GBq activity. The source capsule has a diameter of 5.6 mm, which gives an effective focal spot diameter of 4 mm. A tungsten alloy collimator provides a collimated fan beam with a height of 2 mm and an angle of 46°. The gamma ray detector was placed at a distance of 512 mm from the source. This detector arc comprises 320 contiguously assembled scintillation detector elements each having an active area of 2 mm width and 8 mm height. To increase axial resolution we collimated also the detector to an active height of 3 mm by placing an additional slit collimator in front of the detector arc. With both the source and the detector collimator each ray passing from the source capsule to an individual detector element has a cross-section of approximately 2.6 mm × 2.7 mm. The detector is operated in pulse counting mode with energy discrimination, i.e. incident gamma photons are counted if the deposition energy is within an approximately 240 keV wide window about the photo peak. The detector electronics transfers the count rate data to a measurement PC at user specified time intervals. There, further data processing is carried out. Both energy discrimination and spatial collimation considerably reduce the count rate linearity error that results from counting of scattered photons, which have left the path of a straight line between source and detector and thus lead to errors in the line integral measurement. The spatial resolution of the system is about 0.2 line pairs mm^{-1}. Further details concerning the detector and tomograph design are given by Bieberle et al. [27] and by Hampel et al. [28].

For the experiments in this study the reactor was placed between the source and the detector with its axis at a distance of 350 mm from the source. It is there mounted on a motor-driven and computer-controlled rotational–translational stage and can in this way be moved in a vertical direction and rotated. Prior to the experiments after filling the reactor with catalyst particles or glass beads, respectively, the reactor was mechanically joggled for a few minutes in order to densify the packing and to avoid displacement of particles during measurements. For the tomographic scans, the reactor was rotated at a speed of 0.083 rpm. At this low speed, effects of centrifugal forces on liquid phase can be neglected. This was proven by a preliminary experiment. Here, we inserted both fillings into a cup with a diameter similar to the reactor diameter to a height of about 2 cm, filled up with liquid and added dye droplets at some locations into the bed. We recorded the behavior of the liquid phase during rotation by a high-speed CMOS camera mounted above the cup. No force exertion on the liquid (spreading of the dye area, liquid movement, surface deformations at the gas–liquid phase boundary) was observed.

The trickle bed reactor is projected onto 64 detectors. Thus only the values of the $n_D = 80$ detectors around the projected axis of the reactor were considered for image reconstruction. The number of projections required for image reconstruction should be at least $n_P = \pi d_R/l$ where d_R is the reactor diameter and l the length of the resolution element. With $l \approx 2.5$ mm for the employed CT scanner this gives a value of 113. However, a slight oversampling of $n_P = 200$ was used to increase signal to noise ratio. For each projection counting was performed for 2 s giving approximately 1.6×10^4 cps for those detectors which were not obstructed by the trickle bed reactor and count rates between 3.5×10^3 and 9.0×10^3 cps for the central cord, depending on the type of packing and the phase distribution in the reactor. For each liquid flow rate, initial liquid distributor and packing, full tomographic scans were performed at six different heights (50,

100, 150, 200, 250 and 300 mm downstream from the top of the packing).

3. Data processing

Tomographic data acquisition requires obtaining a number of different data sets. Firstly, a dark count data set $\mathbf{N}^{(\mathrm{d})} = \{N_k^{(\mathrm{d})}\}$ is measured, which gives the number of photoabsorbed gamma photons per unit time in detector k with $k \in [0, n_\mathrm{D} - 1]$ when the source is not in operation. This background signal is approximately 43 cps per detector and mainly comes from the radioactive decay of the lutetium which is one component of the scintillator material. Next, two calibration data sets are acquired by performing full tomographic scans of the reactor. These are the data set $\mathbf{N}^{(\beta=0)} = \{\mathbf{N}_{k,l}^{(\beta=0)}\}$ for the dry packing, i.e. the bed without liquid, and the data set $\mathbf{N}^{(\beta=1)} = \{\mathbf{N}_{k,l}^{(\beta=1)}\}$ for the bed completely filled with liquid. In both data sets β denotes the liquid saturation and l the index of the projection taken at angle $\varphi_\mathrm{m} = 2\pi l/n_\mathrm{P}$, $m \in [0, n_\mathrm{P} - 1]$. Eventually, the trickle bed reactor is scanned for a given flow scenario resulting in a data set denoted by $\mathbf{N}^{(\beta)} = \{\mathbf{N}_{k,l}^{(\beta)}\}$. From these data the linear extinction maps

$$E_{k,l}^{(\beta=1)} = -\log \frac{N_{k,l}^{(\beta=1)} - N_k^{(\mathrm{d})}}{N_{k,l}^{(\beta=0)} - N_k^{(\mathrm{d})}}$$
$$E_{k,l}^{(\beta)} = -\log \frac{N_{k,l}^{(\beta)} - N_k^{(\mathrm{d})}}{N_{k,l}^{(\beta=0)} - N_k^{(\mathrm{d})}} \quad (1)$$

are calculated. They contain the integral values of radiation attenuation due to the presence of liquid for each ray path between the source and detector k at projection l. The extinction data sets are then subjected to the reconstruction procedure. There, the attenuation coefficient maps $\boldsymbol{\mu}^{(\beta=1)} = \{\mu_{i,j}^{(\beta=1)}\}$ and $\boldsymbol{\mu}^{(\beta)} = \{\mu_{i,j}^{(\beta)}\}$ are computed from the measurement data. In this study, they are square maps of size $n_x \times n_y = 128 \times 128$ with pixel indices i and j representing the pixel-averaged attenuation coefficient distribution within an area of 110 mm × 110 mm around the axis of the reactor. Among the applicable reconstruction algorithms we decided to use the algebraic reconstruction technique ART [29]. Though computational effort is higher compared to commonly used backprojection techniques ART offers the advantage of a direct computation of the absolute attenuation maps whereas analytic techniques require proper post-reconstruction scaling of the data due to the non-conservative nature of filter kernels [30]. The ART reconstruction step is given by

$$\mu_{i,j}^{(\tau+1)} = \mu_{i,j}^{(\tau)} + \lambda \frac{E_{k,l} - \sum_{i=0}^{n_x-1}\sum_{j=0}^{n_y-1} a_{i,j,k,l}\mu_{i,j}^{(\tau)}}{\sum_{i=0}^{n_y-1}\sum_{j=0}^{n_x-1} a_{i,j,k,l}^2} a_{i,j,k,l}. \quad (2)$$

where $a_{i,j,k,l}$ denotes the geometric contribution of ray (k, l) to pixel (i, j), τ is the iteration number and λ a relaxation factor, which must be in the range $0 < \lambda \leq 2$. Reconstructions were performed with $\lambda = 1.0$ and $\boldsymbol{\mu}^{(0)} = 0$. Convergence proved to be very fast for the given problem, thus we terminated the computation after 10 iteration steps. For this number of iterations and the comparatively small size of the data map ($n_\mathrm{D} = 80$, $n_\mathrm{P} = 200$) the iterative computation takes only a few seconds on a standard PC which makes its application to this problem feasible.

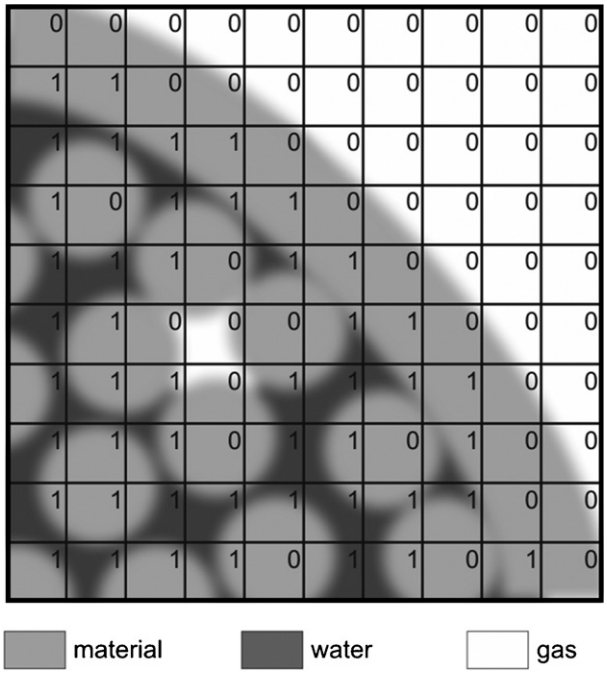

Fig. 2. Illustration of the determination of valid voxels. The image shows a partial map of the reconstructed attenuation coefficient distribution. Voxels, which contain a sufficient portion of liquid, are labelled as valid voxels (1). All other voxels are labelled as invalid voxels (0).

The liquid saturation distribution map $\boldsymbol{\beta} = \{\beta_{i,j}\}$ is eventually computed from the attenuation coefficient maps according to

$$\beta_{i,j} = \frac{\mu_{i,j}^{(\beta)}}{\mu_{i,j}^{(\beta=1)}}. \quad (3)$$

Thereby, $\beta_{i,j}$ is again a discrete representation of the real continuous distribution $\beta(x, y)$ in the scanned plane. The problem with Eq. (3) is that the denominator may become very small. This is the case if the volume element of a corresponding voxel (i, j) is insufficiently covered by liquid when the reactor is flooded. There may be different reasons for such a situation. First, the volume element may be entirely outside the porous space, e.g. in the region of the reactor wall, outside the reactor volume or entirely within a non-porous bead, such as a glass bead. Otherwise gas may be captured in some pores after flooding (see Fig. 2). In such cases, Eq. (3) would result in false and even physically implausible values outside the range $\beta_{i,j} \in [0,1]$. Therefore, we first determine a mask which excludes such voxels from further consideration. The values of this validity mask $\boldsymbol{\nu} = \{\nu_{i,j}\}$ are given by

$$\nu_{i,j} = \begin{cases} 1 & \text{if } \dfrac{\mu_{i,j}^{(\beta=1)}}{\max_{i,j}\{\mu_{i,j}^{(\beta=1)}\}} > \mathrm{th} \\ 0 & \text{otherwise} \end{cases}. \quad (4)$$

Thus, we define a voxel as being valid for consideration in the liquid saturation calculation if the ratio of its attenuation value to

the maximum attenuation value in the image exceeds a threshold th ∈ [0,1]. For this study we chose th = 0.03. The determination of the valid voxels is illustrated graphically in Fig. 2.

Applying this analysis of valid voxels we found that there was a noticeable number of invalid voxels for the glass bed, whereas the porous catalyst bed was completely filled at all locations with liquid during the reference measurement.

Eventually, additional post-processing of the data was performed and the integral liquid saturation as well as radial liquid saturation profiles were calculated on the basis of the data. Since liquid saturation essentially consists of two components, namely, dynamic liquid saturation $\boldsymbol{\beta}^{(\mathrm{dyn})}$, which is the liquid fraction that is being transported through the bed, and static liquid saturation $\boldsymbol{\beta}^{(\mathrm{stat})}$, which is the liquid fraction that is being caught between particles as well as in the porous structure of the catalyst, additional measurements to determine the static saturation were performed separately. Thus, after measuring the total liquid saturation $\boldsymbol{\beta}^{(\mathrm{tot})} = \boldsymbol{\beta}^{(\mathrm{stat})} + \boldsymbol{\beta}^{(\mathrm{dyn})}$ at a certain operation point of the reactor (gas and liquid flow rates) the bed was drained by stopping the liquid supply and tomographic scans were performed in the selected slices about 30 min after stopping the liquid supply. The static liquid saturation was reconstructed in this way from the recorded data. The static liquid saturation and thus the total liquid saturation depends to a great extent on the intraparticle liquid fraction due to the specific particle pore volume, which is approximately 0.65 mL g^{-1} for the catalyst packing and zero for the glass packing. Thus, the dynamic liquid saturation results are separated from measurements and discussed below.

This drainage technique is generally based on the assumption that the static liquid fraction including the liquid content in the catalyst pores is constant and does not change after starting the draining of the packing. To prevent different pore filling levels during the measurement, the porous packing was initially flooded to soak the particles by the liquid phase. Additionally, in a preliminary experiment few particles were soaked in water. The volume of the weighted water in the pore filled particles (dry external surface) is in fair agreement (a bit lower) with the manufacturers' data of the specific pore volume.

4. Results and discussion

4.1. Axial dynamic liquid saturation distribution

Fig. 3 shows exemplarily representative reconstructed cross-sectional dynamic liquid saturation distribution images from the plane 100 mm below the top of the packing. Initial liquid distribution was uniform (spray nozzle) and distributions are shown for both liquid flow rates and both packing types. Dynamic liquid saturation distribution in the glass packing indicates development of liquid channels and regions which are completely separated from the flowing liquid. The number and the dimension of the liquid channels increase with increasing liquid flow rate. At the higher flow rate of 25 L h^{-1} the channels are more widely distributed over the whole cross-section, while at a flow rate of 15 L h^{-1} the channels are located primarily in the wall region. As expected, cross-sectional dynamic liquid saturation

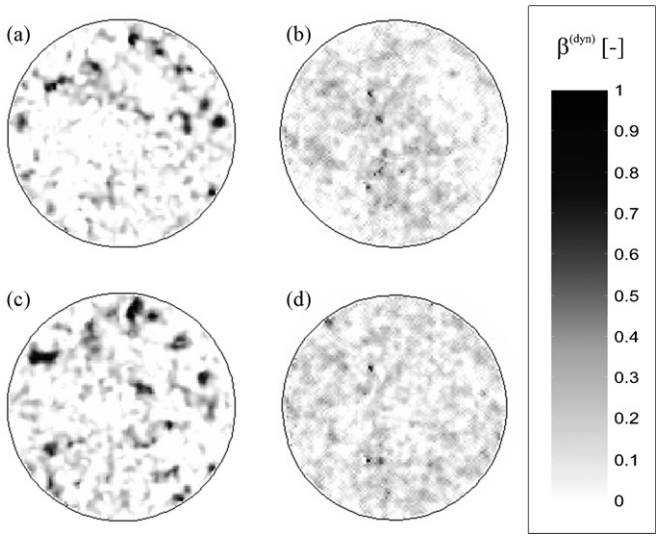

Fig. 3. Dynamic liquid saturation distribution 100 mm downstream the top of the packing ((a) and (c) glass packing; (b) and (d) catalyst packing; (a) and (b) 15 L h^{-1} and (c) and (d) 25 L h^{-1}).

distribution is more uniform in the catalyst packing due to the material porosity. The underlying boosting effect of the porosity is explained in more detail in the Section 4.3. Here, only a few small channels which are more centrally located are indicated.

Integral dynamic liquid saturation values were calculated according to

$$\beta_{\mathrm{int}}^{(\mathrm{dyn})} = \frac{\sum_{i=0}^{n_y-1}\sum_{j=0}^{n_x-1} v_{i,j}\beta_{i,j}}{\sum_{i=0}^{n_y-1}\sum_{j=0}^{n_x-1} v_{i,j}} \tag{5}$$

at each height and for both liquid flow rates and packings. Results are shown in Fig. 4.

Additionally, average dynamic liquid saturation for the whole reactor was calculated by averaging integral dynamic liquid saturation over all heights according to

$$\bar{\beta}^{(\mathrm{dyn})} = \sum_{h=0}^{5} \beta_{\mathrm{int},h}^{(\mathrm{dyn})}. \tag{6}$$

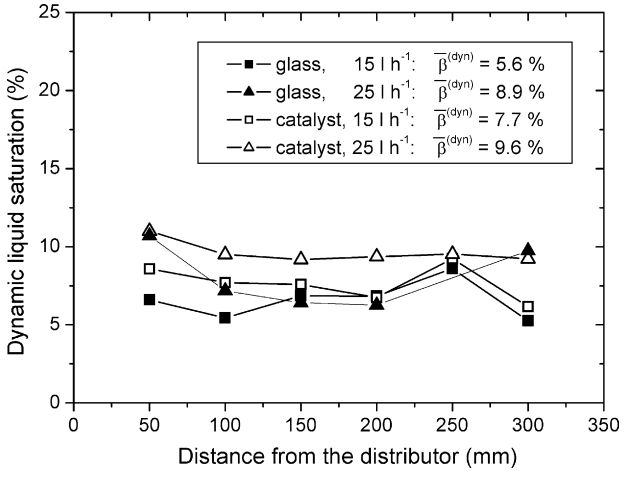

Fig. 4. Dynamic liquid saturation integrated over corresponding cross-section images.

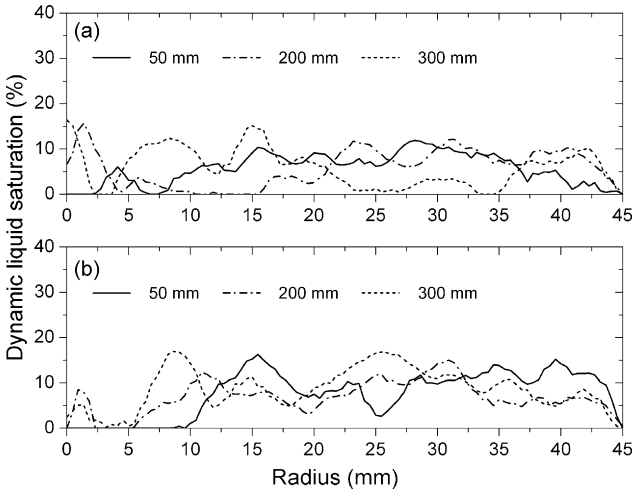

Fig. 5. Radial dynamic liquid saturation profiles at different planes of the glass packing downstream the top of the packing ((a) 15 L h^{-1} and (b) 25 L h^{-1}).

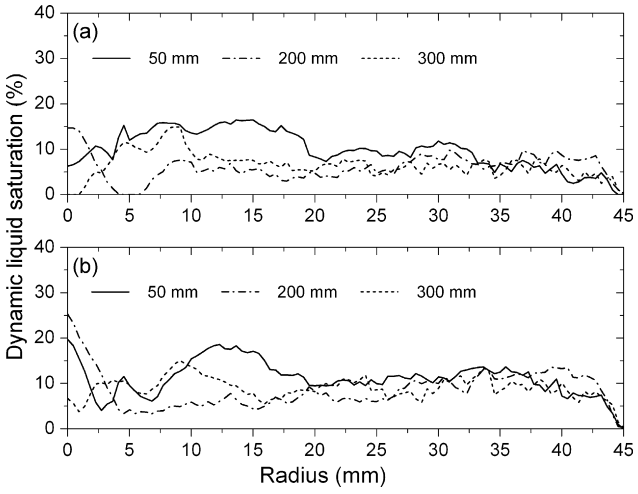

Fig. 6. Radial dynamic liquid saturation profiles at different planes of the catalyst packing downstream the top of the packing ((a) 15 L h^{-1} and (b) 25 L h^{-1}).

Here h denotes the index of the measured slice. Average dynamic liquid saturation values as well as axial profiles of the integral values of the catalyst packing are slightly higher compared to the glass packing at the same flow conditions. Dynamic liquid saturation increases with liquid flow rate for each packing.

Non-uniform dynamic liquid saturation distribution in the glass packing in Fig. 3 is confirmed by more pronounced fluctuation around the average value in Fig. 4, while axial profiles in the catalytic bed show only slightly decreasing dynamic liquid saturation with increasing distance from the liquid distributor. However, since the external bed porosity is expected to decrease slightly with distance from the top of the reactor, e.g. as shown by Boyer et al. [21], it would have been more likely to expect inverse axial dynamic liquid saturation profiles.

4.2. Radial dynamic liquid saturation distribution

Radial dynamic liquid saturation profiles are defined as an average of the dynamic liquid saturation along a circular path with radius r and formally given by

$$\beta^{(\mathrm{dyn})}(r) = \frac{1}{2\pi}\int_0^{2\pi} \beta^{(\mathrm{dyn})}(r\cos\theta, r\sin\theta)\mathrm{d}\theta. \quad (7)$$

Numerical calculation was performed by averaging the values $\beta_{i,j}^{(\mathrm{dyn})}$ of pixels being intersected by a circle of given radius r. Resulting radial profiles for the glass packing and the catalyst packing are shown in Figs. 5 and 6, respectively. It should be noticed that statistical error is higher in the central region due to the decrease in circumference and thus integration area with radius.

Despite uniform initial liquid distribution performed by the spray nozzle, radial profiles show clear fluctuations of the dynamic liquid saturation for both packing materials and both liquid flow rates. While these fluctuations are present over the whole radius in the glass packing, a nearly stable range was observed in the annular region ranging from 20 to 35 mm (Fig. 6). Lower dynamic liquid saturation at the wall region between 40 and 45 mm is in agreement with higher external bed porosity of a randomly packed bed with spherical particles (e.g. [31]).

4.3. Liquid spreading

Additional measurements of the liquid spreading from a central point source were performed in the glass packing and in the catalyst packing. Fig. 7 shows exemplarily the spreading liquid saturation at two different planes downstream from the top of the packing (50 and 150 mm) in the pre-wetted catalyst and glass packing at a flow rate of 25 L h^{-1}. Again, it should be noted that pre-wetted packings were used in this study because non-wetted packings are not employed in continuously operating industrial gas/liquid applications apart from the start-up phase.

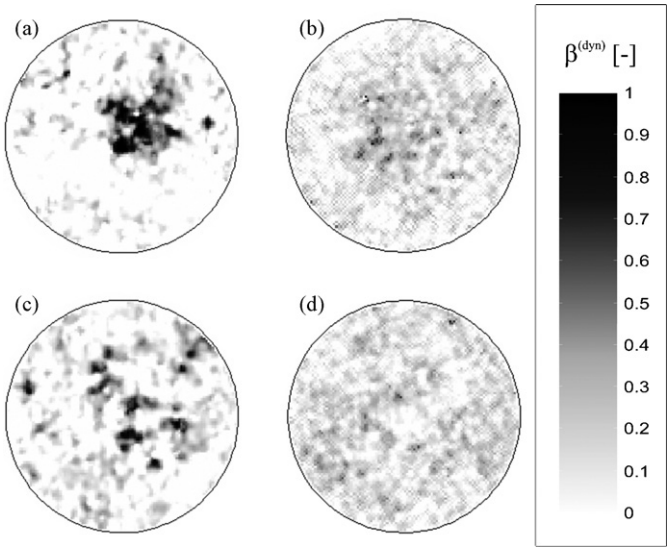

Fig. 7. Liquid spreading of the dynamic liquid saturation at a liquid flow rate of 25 L h^{-1} ((a) and (c) glass packing; (b) and (d) catalyst packing; (a) and (b) 50 mm downstream the top of the packing and (c) and (d) 150 mm downstream the top of the packing).

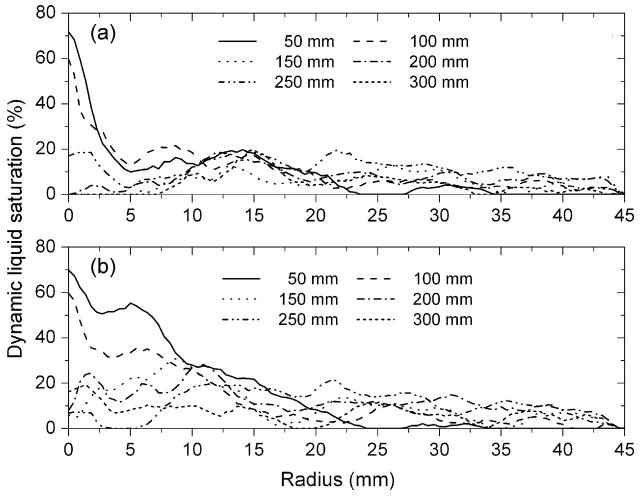

Fig. 8. Dynamic liquid saturation spreading profiles at different planes of the glass packing downstream the top of the packing ((a) 15 L h^{-1} and (b) 25 L h^{-1}).

Liquid spreading with packing length was clearly observed in the glass packing, while in the catalyst packing it is difficult to distinguish between high and low dynamic liquid containing zones as shown in Fig. 7. Radial profiles in all planes for the glass packing and the catalyst packing are shown in Figs. 8 and 9, respectively.

Axial development of the liquid spreading in the glass packing (Fig. 8) shows that the packing radius which is traversed by the dynamic liquid increases in the two upper planes. In the lower planes, the dynamic liquid spreads till to the reactor wall. At planes 200 mm downstream from the top of the packing, a nearly uniform fluctuating dynamic liquid saturation is pronounced. The results are in agreement with Boyer et al. [21] but in contrast to liquid spreading from a point source performed by Ravindra et al. [32]. They reported that even the top layers of the glass beads are covered with liquid due to film flow lateral to the main flow direction in a pre-wetted bed.

Investigation of the liquid spreading in the catalyst packing shows that after 50 mm downstream from the top of the packing more than half of the radius is already passed through by the dynamic liquid fraction. Below 100 mm downstream from the top of the packing, dynamic liquid saturation is almost uniformly distributed over the cross-section, which indicates that there is no central liquid filled channel. It can be assumed that there film flow occurs only over the particles in a pre-wetted porous bed.

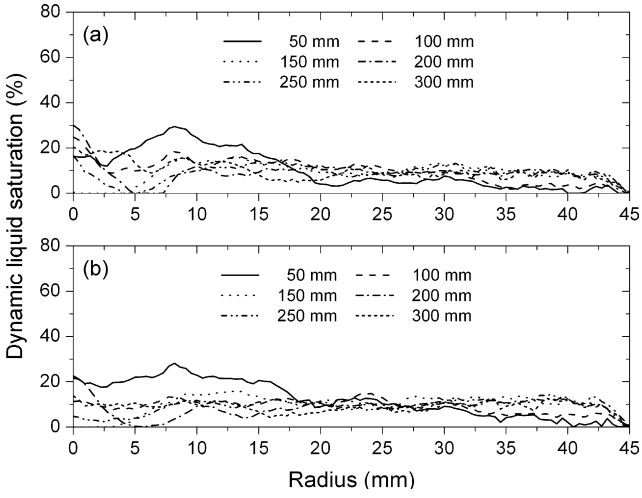

Fig. 9. Dynamic liquid saturation spreading profiles at different planes of the catalyst packing downstream the top of the packing ((a) 15 L h^{-1} and (b) 25 L h^{-1}).

Liquid spreading results using the pre-wetted beds conform with the statement of Maiti et al. [33] given for non-wetted beds that liquid spreading is governed rather by the porosity of the particles than by the contact angle of water over the particle surface. Despite a lower contact angle of water over non-porous glass beads and thus greater expected wettability and stronger liquid spreading, contrary results were obtained. External wetting of the porous catalyst surface leads to internal wetting due to capillary forces and internal wetting leads to more external wetting. This boosting of the external spreading by the presence of liquid filled pores (described in detail in [33]) results in more lateral spreading in a porous bed, even if wettability is lower. Due to low liquid flow rate, the liquid spreading of non-wetted and pre-wetted packings show similar behavior.

5. Conclusion

High-resolution gamma ray tomography has been used and proven its potential to analyze liquid flow textures in a trickle bed reactor both qualitatively and quantitatively. We used for the first time a tomography setup which achieves a spatial resolution of about 2 mm, which is rather high for a photon energy of 662 keV. But due to the random structure of the bed the liquid channels and pores are smaller than the spatial resolution elements which means that only fractional liquid phase can be reconstructed locally. Therefore, we applied proper calibration measurements on empty, flooded and drained beds to obtain quantitative liquid saturation measurements both for static and dynamic holdup.

With the experimental study, we were able to analyze the maldistribution of the dynamic liquid holdup for a spray nozzle producing a uniform initial distribution and a point source distributor producing a central liquid stream in both glass bead bed and porous catalyst bed.

For the glass bed we identified well developed liquid channels and totally dry regions in the cross-sections at every plane downstream from the spray nozzle. In the catalyst packing cross-sectional dynamic liquid saturation distribution has been found nearly uniform which is attributed to the boosting effect of the porosity.

Liquid spreading from a point source was clearly observed in the glass packing, while in the catalyst packing after an entrance region with a length-to-diameter-ratio of about one, dynamic liquid saturation is almost uniformly distributed over the cross-section.

The very different hydrodynamic behavior of the non-porous glass beads and real catalyst particles with porous Al_2O_3 support suggest that a bed of glass beads is not representative for catalytic packings and should not be used for the study of hydrodynamics in such columns as regrettably done in many studies.

In the future, gamma ray studies will be extended for investigations of liquid distribution and liquid spreading for modern high efficiency packing material such as cylindrical extrudates, pall rings and trilobe shaped material of different internal porosity.

References

[1] R.A. Meyers, Handbook of Petroleum Refining Processes, second ed., McGraw-Hill, New York, 1996.

[2] M.P. Dudukovic, F. Larachi, P.L. Mills, Multiphase reactors revisited, Chem. Eng. Sci. 54 (1999) 1975–1995.

[3] I. Harter, C. Boyer, L. Raynal, G. Ferschneider, T. Gauthier, Flow distribution studies applied to deep hydro-desulfurization, Ind. Eng. Chem. Res. 40 (2001) 5262–5267.

[4] R. Krishna, S.T. Sie, Strategies for multiphase reactor selection, Chem. Eng. Sci. 49 (1994) 4029–4065.

[5] M.P. Dudukovic, Opaque multiphase reactors: experimentation, modeling and troubleshooting, Oil Gas Sci. Tech. (Rev. IFP) 54 (2) (2000) 135–158.

[6] M.I. Urseanu, J.G. Boelhouwer, H.J.M. Bosman, J.C. Schroijen, G. Kwant, Estimation of trickle-to-pulse flow regime transition and pressure drop in high-pressure trickle bed reactors with organic liquids, Chem. Eng. J. 111 (1) (2005) 5–11.

[7] Z.E. Ring, R.W. Missen, Trickle-bed reactors. Tracer study of liquid holdup and wetting efficiency at high temperature and pressure, Can. J. Chem. Eng. 69 (4) (1991) 1016–1020.

[8] C. Marcandelli, A.S. Lamine, J.R. Bernard, G. Wild, Liquid distribution in trickle-bed reactor, Oil Gas Sci. Tech. (Rev. IFP) 55 (4) (2000) 407–415.

[9] A.V. Sapre, D.H. Anderson, F.J. Krambeck, Heater probe technique to measure flow maldistribution in large scale trickle bed reactors, Chem. Eng. Sci. 45 (8) (1990) 2263–2268.

[10] L.F. Gladden, M.H.M. Lim, M.D. Mantle, A.J. Sederman, E.H. Stitt, MRI visualisation of two-phase flow in structured supports and trickle-bed reactors, Catal. Today 79–80 (2003) 203–210.

[11] I.V. Koptyug, A.A. Lysova, R.Z. Sagdeev, V.A. Kirillov, A.V. Kulikov, V.N. Parmon, In situ MRI of the structure and function of multiphase catalytic reactors, Catal. Today 105 (2005) 464–468.

[12] H.S. Tapp, A.J. Peyton, E.K. Kemsley, R.H. Wilson, Chemical engineering applications of electrical process tomography, Sens. Actuators B 92 (2003) 17–24.

[13] J. Chaouki, F. Larachi, M.P. Dudukovic, Noninvasive tomographic and velocimetric monitoring of multiphase flows, Ind. Eng. Chem. Res. 36 (1997) 4476–4503.

[14] C. de Vuono, P.A. Schlosser, F.A. Kulacki, P. Munshi, Design of an isotopic CT scanner for two phase flow measurements, IEEE Trans. Nucl. Sci. NS-27 (1) (1980) 814–820.

[15] S.B. Kumar, D. Moslemian, M.P. Dudukovic, A γ-ray tomographic scanner for imaging voidage distribution in two-phase flow systems, Flow Meas. Instrum. 6 (1) (1995) 61–73.

[16] K.A. Shollenberger, J.R. Torczynski, D.R. Adkins, T.J. O'Hern, N.B. Jackson, Gamma-densitometry tomography of gas holdup spatial distribution in industrial-scale bubble columns, Chem. Eng. Sci. 52 (13) (1997) 2037–2048.

[17] U.P. Veera, Gamma ray tomography design for the measurement of holdup profiles in two-phase bubble columns, Chem. Eng. J. 81 (1–3) (2001) 251–260.

[18] H.V. Kok, T.H.J.J. van der Hagen, R.F. Mudde, Subchannel void-fraction measurements in a 6×6 rod bundle using a simple gamma-transmission method, Int. J. Multiphase Flow 27 (1) (2001) 147–170.

[19] H.-M. Prasser, D. Baldauf, J. Fietz, U. Hampel, D. Hoppe, C. Zippe, J. Zschau, M. Christen, G. Will, Time resolving gamma-tomography for periodically changing gas fraction fields and its application to an axial pump, Flow Meas. Instrum. 14 (3) (2003) 119–125.

[20] C. Boyer, B. Fanget, Measurement of liquid flow distribution in trickle bed reactor of large scale diameter with a new gamma-ray tomographic system, Chem. Eng. Sci. 57 (2002) 1079–1089.

[21] C. Boyer, A. Koudil, P. Chen, M.P. Dudukovic, Study of liquid spreading from a point source in a trickle bed via gamma-ray tomography and CFD simulation, Chem. Eng. Sci. 60 (2005) 6279–6288.

[22] Z. Wang, A. Afacan, K. Nandakumar, K.T. Chuang, Porosity distribution in random packed columns by gamma ray tomography, Chem. Eng. Process. 40 (2001) 209–219.

[23] F. Yin, A. Afacan, K. Nandakumar, K.T. Chuang, Liquid holdup distribution in packed columns: gamma ray tomography and CFD simulation, Chem. Eng. Process. 41 (2002) 473–483.

[24] V. Alopaeus, K. Hynynen, J. Aittamaa, A cellular automated model for liquid distribution in trickle bed reactors, Chem. Eng. Sci. 61 (2006) 4930–4943.

[25] R. Khanna, K.D.P. Nigam, Partial wetting in porous catalysts: wettability and wetting efficiency, Chem. Eng. Sci. 57 (2002) 3401–3405.

[26] W. van der Merwe, W. Nicola, F. de Beer, Trickle flow distribution and stability by X-ray radiography, Chem. Eng. Sci. 132 (2007) 47–59.

[27] A. Bieberle, J. Kronenberg, E. Schleicher, U. Hampel, Design of a high-resolution gamma-ray detector module for tomography applications, Nucl. Instrum. Methods Phys. Res., Sect. A 572 (2007) 668–675.

[28] U. Hampel, A. Bieberle, D. Hoppe, J. Kronenberg, E. Schleicher, T. Sühnel, F. Zimmermann, C. Zippe, High-resolution gamma ray tomography scanner for flow measurement and non-destructive testing applications, Rev. Sci. Instrum. 78 (103704) (2007) 1–9.

[29] R. Gordon, R. Bender, G.T. Herman, Algebraic reconstruction techniques (ART) for three-dimensional electron microscopy and X-ray photography, J. Theor. Biol. 29 (3) (1970) 471–481.

[30] C. Kak, M. Slaney, Principles of Computerized Tomographic Imaging, IEEE Press, New York, 1988.

[31] D. Vortmeyer, J. Schuster, Evaluation of steady flow profiles in rectangular and circular packed beds by a variational methods, Chem. Eng. Sci. 38 (1983) 1691–1699.

[32] P.V. Ravindra, D.P. Rao, M.S. Rao, Liquid flow texture in trickle bed reactors, Ind. Eng. Chem. Res. 36 (1997) 5133–5145.

[33] R.N. Maiti, R. Khanna, P.K. Sen, K.D.P. Nigam, Enhanced liquid spreading due to porosity, Chem. Eng. Sci. 59 (2004) 2817–2820.